Quantitative evaluation of mask phase defects from through-focus EUV aerial images

Iacopo Mochi[*a], Kenneth A. Goldberg[a], Ryan Xie[b], Pei-Yang Yan[c], Kenji Yamazoe[d]

[a]Lawrence Berkeley National Laboratory, 1 Cyclotron Road, Berkeley, CA 94120.
[b]Berkeley Sensors and Actuator Center, University of California, Berkeley, CA 94720.
[c]Intel Corp, 2200 Mission College Blvd. Santa Clara, CA 95054.
[d]Canon Inc. 23-10 Kiyohara-Kyogyodanchi Utsunomiya, Tochigi, 321-3298, Japan.

ABSTRACT

We present an improved method of phase retrieval from through-focus image series with higher precision and reduced sensitivity to noise. The previous method, developed for EUV, actinic mask measurements, was based on the Gerchberg-Saxton algorithm and made use of two aerial images recorded in different focal planes. The new technique improves the reconstruction uncertainty and increases the convergence speed by integrating information contained in multiple images from a through focus series. Simulations characterize the new technique in terms of convergence speed, accuracy and stability in presence of photon noise. We have demonstrated the phase-reconstruction method on native, mask-blank phase defects and compared the results with phase predictions made from AFM data collected after the multilayer deposition. Measurements show that a defect's top-surface height profile is not a reliable predictor of phase change in all cases. The method and the current results can be applied to improve defect modeling and to enhance our understanding of the detectability and printability of native phase defects.

Keywords: Extreme ultra violet, mask, phase defect, reconstruction.

1. INTRODUCTION

Mask defects inspection and imaging is one of the most important issues for any pattern transfer lithography technology. This is especially true for EUV lithography where the wavelength-specific properties of masks and defects necessitate actinic inspection for a faithful prediction of defect printability and repair performance.

In this paper we will present a technique to obtain a quantitative characterization of the complex amplitude of mask defects from a series of EUV aerial images recorded with a high-resolution EUV microscope. We apply this technique to measure the aerial image phase of native defects on a blank mask, recorded with the SEMATECH Berkeley Actinic Inspection Tool (AIT), an EUV zoneplate microscope that operates at Lawrence Berkeley National Laboratory. The measured phase is compared with predictions made from AFM top-surface measurements of those defects.

While amplitude defects are usually easy to recognize and quantify with standard inspection techniques like scanning electron microscopy (SEM), defects or structures that have a phase component for EUV wavelengths can be much more challenging to inspect. A phase defect can originate from the substrate or from any level of the multilayer. In both cases its effect on the reflected field is not directly related to the local topography of the mask surface, but depends on the deformation of the multilayer structure.

Using the AIT, we have previously showed that EUV inspection provides a faithful and reliable way to predict the appearance of mask defect on the printed wafer[1]; but to obtain a complete characterization of defects, to improve printability estimates or the success of repair strategies, we need to quantitatively evaluate their full complex amplitude.

While aerial imaging does not provide a direct measurement of the phase of the object, that information is encoded in the through-focus evolution of the image intensity distribution. Recently we developed a technique that allows us to extract the complex amplitude of EUV mask defects using two aerial images from different focal planes.[2]

---

[*] imochi@lbl.gov phone 1 510 486 6921; fax 1 510 486 4955; CXRO — Lawrence Berkeley National Laboratory.

The method for the phase reconstruction is derived from the Gerchberg–Saxton (GS) algorithm, [3,4] an iterative algorithm that can be used to reconstruct an object's phase and amplitude from the intensity distributions in the image and in the pupil plane. We have now modified our two-image complex amplitude reconstruction algorithm to use an arbitrary number of through-focus images, and we compare its performance with the previous version in terms of convergence speed, robustness and accuracy.

1.1 The AIT microscope

The SEMATECH Berkeley Actinic Inspection Tool (AIT) is a synchrotron-based Fresnel zoneplate microscope dedicated to EUV mask imaging. The microscope is an all-EUV instrument featuring an array of selectable objective zoneplate lenses with different numerical apertures and magnifications. The illumination wavelength is tunable between 13.2 and 13.6 nm and the partial coherence has been estimated to be $0.15 < \sigma < 0.2$. Detailed descriptions of the AIT and its performance have been published previously. [5,6] To collect through-focus measurements, the AIT uses a wavelength-shifting technique[7] to change the zoneplate's focal length through small, well-controlled increments.

For simplicity the AIT can be modeled as a simple on-axis circular lens, with coherent illumination. The role of partial coherence in the accuracy of this analysis is a topic of ongoing research beyond the scope of this paper.

1.2 Phase in the aerial images

The finite numerical aperture of the imaging system acts like a low-pass filter on the spatial frequencies of the electric field in the object plane since light from the highest spatial-frequencies falls outside the entrance pupil aperture and is blocked. The same principle applies to phase objects: a phase bump in the object plane may show a smoother profile and a lower peak phase in the image plane as a consequence of its slope and of the numerical aperture of the imaging system.

Many of the phase defects encountered on blank masks can be approximated as Gaussian pits or bumps, for this reason we modeled a pit-like defect with a Gaussian profile and we calculated the expected peak phase in the aerial image for a few different cases. Note that a pit defect behaves like a depression in the mask surface and in our convention it corresponds to a local positive phase difference.

In Figure 1 we show the expected peak phase in the aerial image for pit-like defects of constant, $\pi/2$ phase peak shift on the mask, and various full-width at half-maximum (FWHM) values. Calculations are made for several different NA values. Increasing FWHM decreases the peak slope of the defect's phase profile. In the single-surface approximation of the mask's reflectivity[8] the $\pi/2$ phase change corresponds to a depth of 1.68 nm at 13.4-nm wavelength.
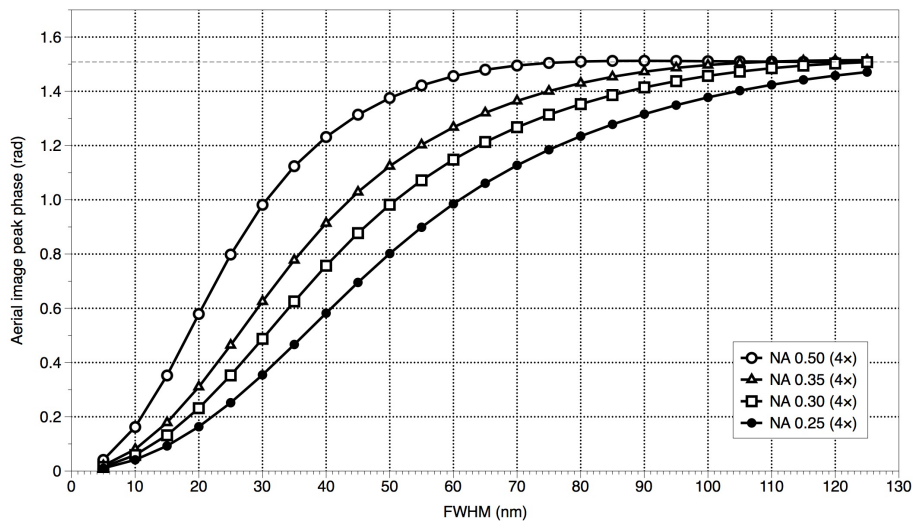

Figure 1. Aerial image peak phase behavior as a function of the FWHM for a Gaussian shaped phase defect with peak phase of $\pi/2$ and a wavelength $\lambda = 13.4$ nm. For smaller defects and lower NA values, the peak image phase is reduced relative to the input object phase change on the mask. In particular, the lower curve (0.25 NA 4×) corresponds to the imaging data shown in this paper.

For convenience we reference all NA values assuming the 4× demagnification used in conventional steppers. Mask-side NA values are 4 times smaller than their wafer-side equivalent.
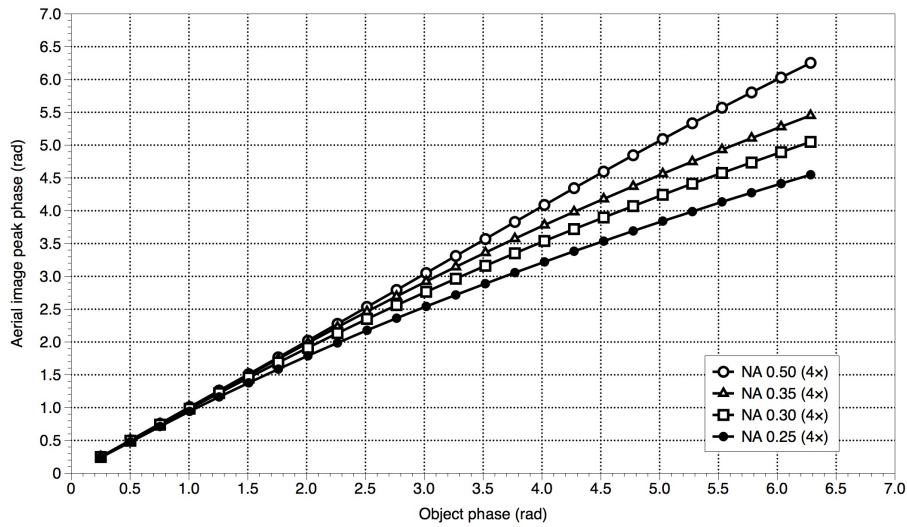

Figure 2. Aerial image peak phase behavior as a function of the peak phase change on the mask, for Gaussian-shaped phase defects with a fixed FWHM of 100 nm and 13.4-nm wavelength.

2. PHASE RECONSTRUCTION ALGORITHM

We have previously reported a method to reconstruct the complex amplitude of an aerial image from the intensity recorded in two different focal planes near best focus.[2] The method is based on the Gerchberg-Saxton (GS) algorithm, which was originally developed to use the amplitude in the pupil and in the image plane. Our algorithm uses two images in arbitrary focal planes and does not require measurement in the pupil-plane, which is not always easily accessible. The method was successfully tested on a EUV phase shifting mask, and we used it to study native phase defects on blank and patterned masks.

Despite the complexity of the problem, the GS algorithm is analogous to a two-parameter optimization problem: it needs exactly two constraints to be solved. The measured intensity distributions in two different focal planes supply that constraint. We also use knowledge of the finite pupil aperture size as an additional constraint. In some formulations, adding an additional constraint (i.e. more images) would result in an ill posed problem.[9] On the other hand, we have observed that the solution's stability and convergence time during computation can both be improved using more information, especially in the presence of noise. We modified our reconstruction algorithm to work with an arbitrary number of through focus images and demonstrate that through-focus image series recorded with the AIT can be used to recover the complex amplitude of the aerial image.

2.1 Generic multi-image phase reconstruction

The phase reconstruction algorithm diagrammed in the flow-chart of Fig. 3, consists of four steps.

The first step is to create an initial phase profile for each of the images. If there is no information on the structure of the object under investigation, a constant zero phase or a uniformly distributed random phase array with values between $-\pi$ and π are two equally valid options. The initial phase guess P_0 for the aerial image in focus is used to create an array of phase maps $\{P_n\}$ for all the images in the series. Using $\{P_n\}$ and the series of recorded intensities $\{I_n\}$, we can create an array of complex amplitudes C.

$$C_n = \sqrt{I_n} \exp(iP_n),$$

(1)

where P_n is the aerial image phase guess for the n-th defocus plane.

Step number two propagates the field from each focal plane into the pupil. Here we apply a Fourier transform to each element of the array C and then remove the defocus term as follows.

$$B_n = \text{FFT}(C_n) \, \exp(-iD_n). \tag{2}$$

D_n is the defocus term to get from the image plane to the *n*-th defocus plane and it is described by:

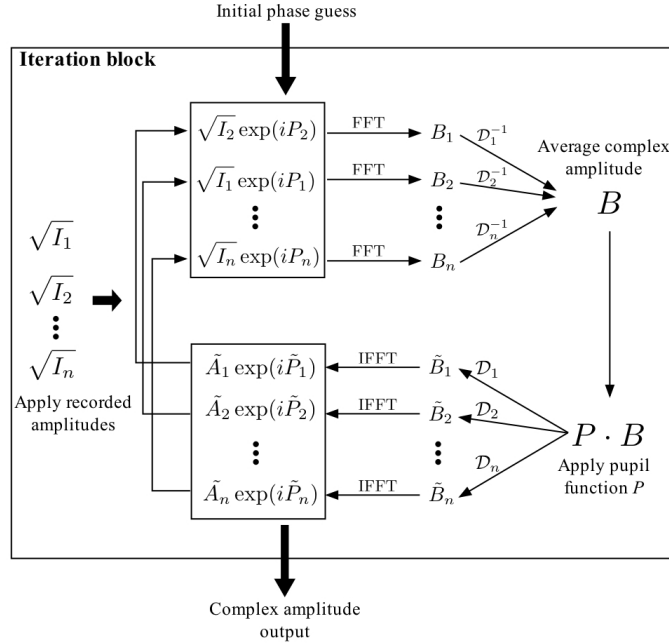$$D_n(x,y) = a_n \left[2(\tilde{x}^2 + \tilde{y}^2) - 1\right]. \tag{3}$$

Figure 3. Flow-chart of the generic multi-image phase reconstruction algorithm. The operator D_n is used to add and subtract the necessary amount of defocus to propagate the complex amplitude from the focal plane to the n-th out of focus plane.

where $\tilde{x}$ and $\tilde{y}$ are normalized to the pupil radius, and the coefficient a_n depends on the object side numerical aperture *NA,* the wavelength λ and the longitudinal distance δ_n of the object from the focal plane:

$$a_n = \pi \, \delta_n NA^2 / \lambda. \tag{4}$$

Here, a_n is calculated in the paraxial approximation.[10]

We estimate the complex amplitude in the pupil plane B by calculating the weighted average of the amplitudes obtained from the different planes B_n. While the choice of weighting function could depend on the relative signal to noise ratio in the images and on the partial coherence of the imaging system, we select equal weights with unit magnitude.

Step number three is to apply the pupil function P to the complex amplitude B and propagate it back to the focal planes of the recorded images. Since the pupil physically removes spatial frequencies above a given cutoff, applying the pupil function forces the reconstructed images to adhere to the physical constraints of the imaging system. The calculation is performed by re-introducing the defocus phase and applying an inverse Fourier-transform.

$$\tilde{C}_n = \text{IFFT}\left[P \cdot B \exp(iD_n)\right] = \tilde{A}_n \exp(i\tilde{P}_n) \tag{5}$$

where $\tilde{A}_n$ and $\tilde{P}_n$ are the reconstructed amplitude and phase in the *n*-th focal plane.

Step number four consists of applying the recorded amplitude constraint to each of the complex amplitudes $\tilde{C}_n$. This is done by substituting the calculated amplitude, $\tilde{A}_n$, with the known amplitude A_n, obtained from the square root of to the measured intensity, I_n. In this step, the calculated phase is preserved.

Steps 2 to 4 are iterated until a specific convergence condition is met. A simple way to evaluate the quality of the reconstruction is to compare the reconstructed amplitudes $\tilde{A}_n$ and the measured ones A_n. For example, the iterative process can be stopped when the root mean square difference of the two sets of amplitudes reaches the desired threshold. Alternatively, iterations can be stopped when the maximum phase-change from one cycle to the next drops below a given threshold, or when a given number of iterations has been reached.

2.2 Simulations of noise-induced error.

To study the effect of aerial image photon noise on the phase reconstruction, we have run simulations with increasing photon densities and different numbers of images used in the reconstruction. We modeled a Gaussian-shaped phase defect whose complex amplitude on the mask surface is given by:

$$C(x,y) = A(x,y) \exp[iP(x,y)]. \tag{6}$$

In this case the amplitude A is uniform with unit magnitude, while the phase profile P is described by:

$$P(x,y) = p \ \exp[-(x^2 + y^2)/2\sigma^2], \tag{7}$$

where p is the peak phase and the *FWHM* is equal to 2.3 σ.

In this study, we chose p equal to π and a *FWHM* of 100 nm. In the single surface approximation, this choice corresponds to a pit defect with a depth of 3.35 nm. In the simulations we used a numerical aperture of 0.0625 (4× NA of 0.25), a wavelength of 13.4 nm and an effective pixel size of 15 nm to match the physical parameters of the experiment described in this paper. We generated a simulated through-focus image series by propagating the complex amplitude on the surface of the mask to different focal planes, choosing the defocus step size to match 0.4 μm of mask z translation. We calculated the intensity of each image and we added random noise following the Poisson distribution to simulate increasing photon densities from 5 to 2000 photons/pixel. We ran the reconstruction algorithm for a fixed amount of iterations to reconstruct the phase of the aerial image in the focal plane. To estimate the accuracy of the reconstruction we compared the phase of the simulated aerial image in the focal plane P_0 and the reconstructed phase P_r, over an area S of 180×180 nm^2, corresponding to $N = 144$ pixels, centered on the defect peak. We defined the RMS phase error Pe as:

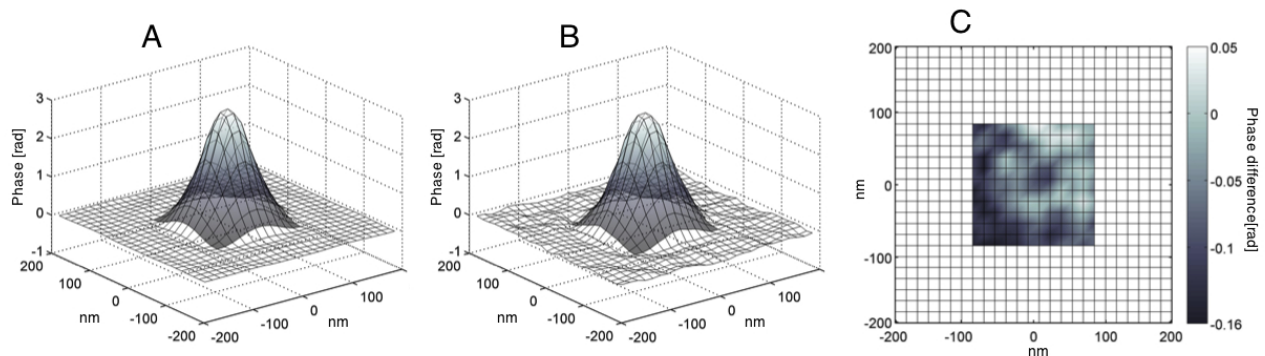$$Pe = \sqrt{\sum_S \left[P_0(x,y) - P_r(x,y) \right]^2 \Big/ N}. \tag{8}$$

Figure 4. **(A)** is the aerial image phase profile of the Gaussian pit defect that we used in the simulation. The peak phase is 2.92 rad, the FWHM is equal to 92.70 nm. The shaded area represents the 180×180 nm area that we used to evaluate *Pe*. **(B)** is the phase profile reconstructed using 7 images and a photon density of 100 photons/pixel. **(C)** is the difference between the reconstructed phase profile and the original one.

We repeated the simulation 50 times and we defined the uncertainty of the phase reconstruction as the average RMS phase error. Given this defect and simulation model, we investigated the effect of using different numbers of images in the reconstruction by repeating the same simulation for various images series. To make a practical comparison of the results we chose to keep constant the number of Fourier pairs evaluated in each reconstruction. One iteration of the

algorithm involves the calculation of one Fourier pair for each image in the series (see Fig. 3). After 22000 Fourier pair evaluations, for any image number, the solution was stable to within ±0.02 rad (RMS). This corresponds to ~7300 iterations using a three image series and to ~3000 iterations using seven image series. The execution time depends on the image array size and on the platform used to run the reconstruction. In our case we used a 54×54 pixel array and a 2008 commercial laptop with a 2.53 GHz dual-core processor. The average reconstruction time was ~30 s.

As shown in Fig. 5, the simulation results demonstrate a clear advantage in using a higher number of images, especially in the case of low photon densities (i.e. high noise). In the assumption that photon shot noise is the only significant noise source, a photon density of 100 photons/pixel corresponds to signal to noise ratio of 10 and in this case the simulations show that there is a 35% improvement in the average phase RMS error by using seven images instead of three.
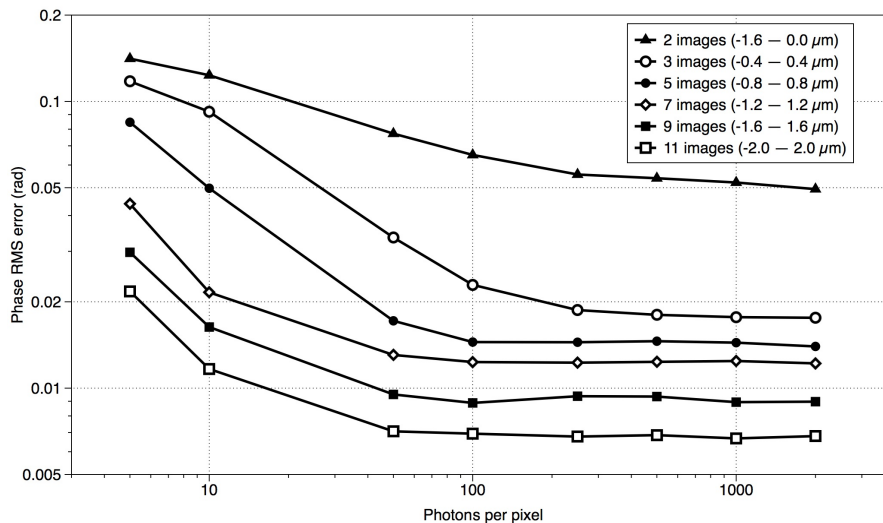

Figure 5. RMS phase error after 22,000 Fourier-pair evaluations are shown as a function of photon density, for series than include 2 to 11 images. All the images in the series have 0.4 ⌈m through-focus step size. The highest curve represents the error in the reconstruction performed using the original, two-image version of the algorithm, which used one image from the focal plane and one image 1.6 μm out of focus.

3. NATIVE DEFECTS PHASE RECONSTRUCTION

We used the multi-image reconstruction method to measure the aerial image phase of a set of native defects on a blank mask provided by Intel. All the defects inspected with the AIT showed a strong phase behavior, which can be compared with the phase predicted by atomic-force microscope (AFM) measurements of the top surface measurements. Many of the defects measured in the AFM, could be well approximated with a Gaussian shape. (see for example Fig. 6A).

3.1 AIT images pre-processing

To extract the aerial image intensity from the raw CCD images in the AIT, we must perform several steps. The standard pre-processing procedure for the AIT images requires subtracting the background (CCD offset), interpolating and rotating the image, and normalizing the image intensity to correct for illumination non-uniformities.

Since the AIT is an off-axis system, images collected through focus appear to move away from the optical axis. While this effect is predictable and can be corrected, we find that there is a small residual instability in the lateral position of the projected image (up to several pixels). Unintentional lateral image shifts through focus are interpreted by the reconstruction algorithm as a tilt in the phase component. More specifically, if only two images are used, any lateral misalignment between them will be reconstructed as a phase difference. Using a series with more than two images randomly misaligned will result in an inconsistent set of Fourier transform pairs and in a larger reconstruction error. To minimize this effect we pre-align the images by minimizing the RMS intensity difference of the sequential image pairs. The alignment works under the assumption that adjacent images in the series have a comparable shape. To meet this condition, the image series collected to perform the complex amplitude reconstruction have an equivalent through focus step size of 0.4 μm, the smallest allowed by the system. We recognize that this alignment method may not work well for large z steps between series images.

3.2 AFM-based estimate of the phase in the aerial image

The aerial image phase of the defects can be estimated from their topography using the single-surface approximation.[8] First, we use the AFM profile to calculate the phase change induced by the defect, P_s, based on its surface depth on the mask, $h(x, y)$.

$$P_s(x,y) = 2h(x,y) \cdot 2\pi / \lambda. \tag{9}$$

Assuming that the surface disturbance causes a pure phase change and the local reflectivity of the mask $A(x, y)$ remains constant, we propagate the complex amplitude on the surface of the mask to the aerial image plane, simulating a perfect lens with a mask-side NA of 0.0625, to reproduce the effect of the AIT zoneplate used to inspect the defects. As we described in Section 1.2, we observe a reduction in the slope and a decrease in the magnitude of the peak phase.
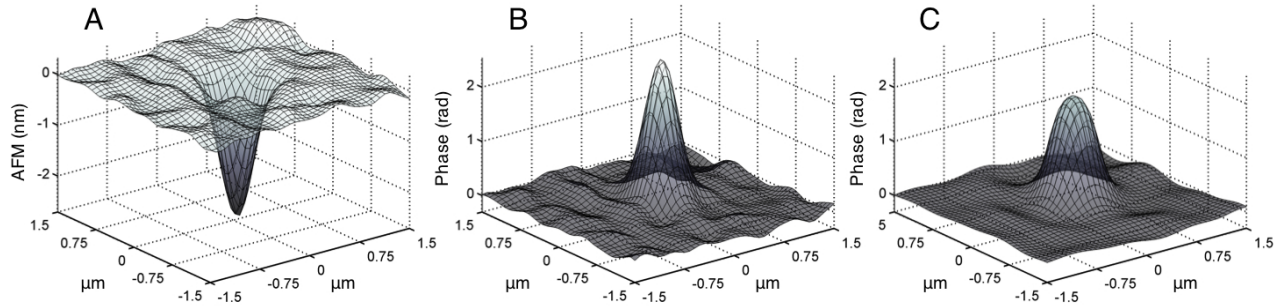

Figure 6. **(A)** shows an example of the measured AFM profile of a pit defect with a peak depth of 2.75 nm. The FWHM was measured assuming a rotationally symmetric profile, is equal to 72 nm. **(B)** represents the defect phase on the surface of the mask, P_s, calculated using Eq. 9. In this case the peak phase is equal to 2.58 rad. **(C)** is the estimated phase profile in the aerial obtained using an mask-side NA equal to 0.0625. Here the peak phase and FWHM are 1.90 rad and 90 nm, respectively.
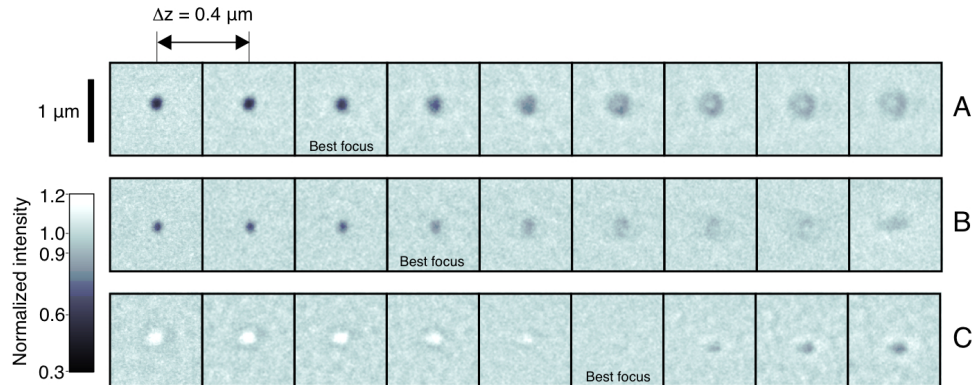

Figure 7. Examples of through-focus aerial image series, collected with the AIT. **(A)** shows a pit defect with an AFM peak depth of 12 nm and a FWHM of 73 nm. **(B)** shows a pit defect with an AFM peak depth of 2 nm and a FWHM of 82 nm. **(C)** shows a bump defect with an AFM peak depth of -1 nm and a FWHM of 224 nm.

The nineteen defects we inspected have a wide range of depth and FWHM, nonetheless its useful to notice that the mean FWHM of the defects' AFM profile is 92 nm and, after the propagation, the mean FWHM of the phase profile is 108 nm consistently with the smoothing expected from the lens spatial filtering effect.

3.3 Complex amplitude reconstruction of native defects

We inspected and reconstructed nineteen phase defects on a blank mask provided by Intel. For each defect we recorded a through focus image series with focal step size of 0.4 µm.

Finding focus on a blank mask surface is not straightforward since there are no amplitude structures to rely upon. To estimate the best focal position we observed the behavior of the contrast induced by the mask surface phase roughness which is present on all masks we have observed.[11] It can be demonstrated that this contrast reaches a minimum when the mask surface is in focus.[12] The high spatial coherence of the AIT illumination ($\sigma \sim 0.2$) allows us to clearly observe this effect and use it to determine the best focus plane within about 0.2 μm, half of the minimum through focus step size of the system. Within each through-focus series, we identified the best focus image, and selected a sub-series of 7 images centered on it to reconstruct the phase. We limited to seven the number of images on each series because it was the highest value available for all the defects.

The photon density in the AIT images is controlled changing the exposure time. We have calculated that about 441 photons/pixel are required to overcome shot noise and record line edge roughness measurement (10% CD at 22 nm half-pitch),[13] but as shown in Fig. 5, it takes considerably less to obtain a good accuracy in the phase reconstruction. In the images used in this analysis, typical intensity levels provide approximately 250 photons/pixel per image, with an effective pixel width that is more than four times smaller than the diffraction-limited resolution.
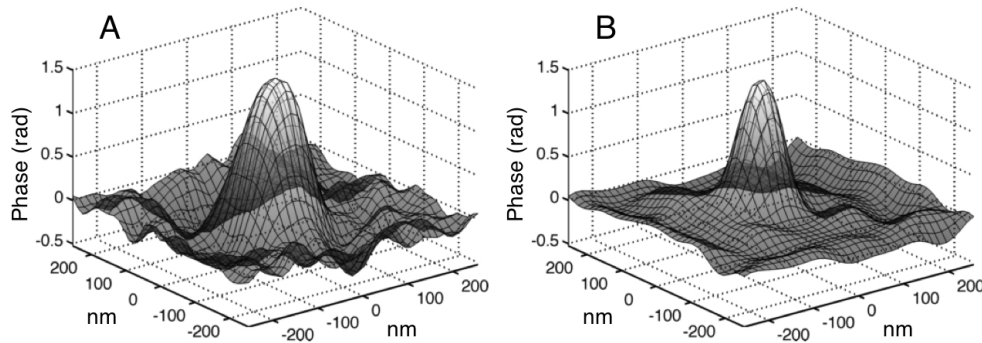

Figure 8. **(A)** is the reconstructed phase profile for the defect shown in Fig. 7B, calculated with 7 images. The peak phase of the reconstructed profile is 1.512 rad and the FWHM is 129 nm **(B)** is the phase profile of the same defect estimated from the AFM data in the single-surface approximation. The peak phase here is 1.507 rad and the FWHM is 99 nm.
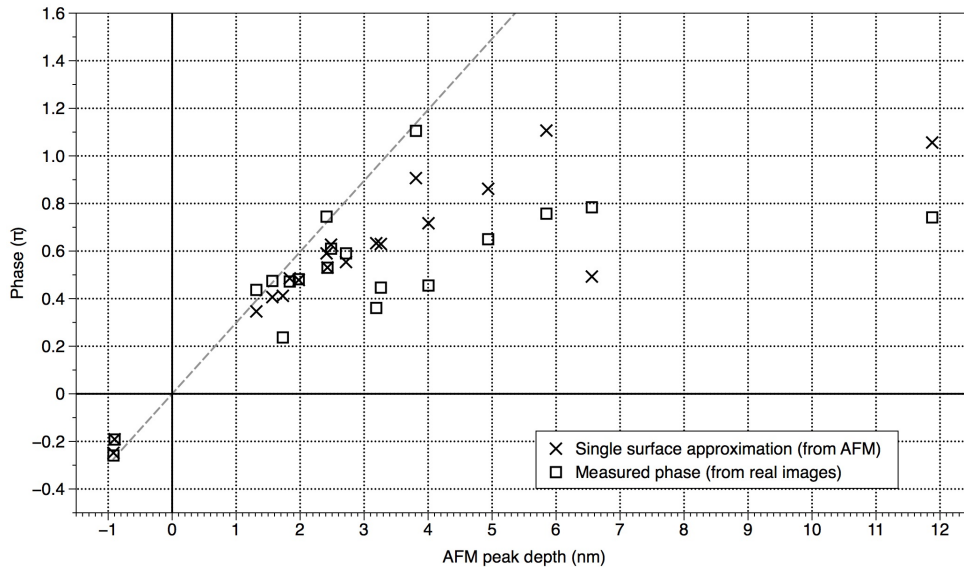

Figure 9. In this plot we show the comparison between the aerial image peak phase of the defects predicted from the AFM measurements and the value obtained from the complex amplitude reconstruction performed using 7 through focus images with a 0.4 mm focal step size. On the horizontal axis we reported the measured depth of the defects, therefore pits and bumps are in the positive and negative x region respectively. The dashed line shows the estimated peak phase of the defects on the surface of the mask, calculated with Eq. 9.

We let the phase reconstruction algorithm run for 3000 iterations, corresponding to 21000 Fourier pair evaluations. At this point the RMS phase variation rate was lower than 0.02 rad/iteration and a stable solution had emerged. For the defect shown in Fig. 7B, Fig. 8 shows a side-by-side comparison of the aerial image phase profiles calculated (A) from the AFM data using the single-surface approximation and (B) from the phase reconstruction algorithm using 7 images.

Figure 9 shows a comparison between the aerial image phase peak values calculated from the AFM data (single-surface approximation), and from the phase reconstruction algorithm (based on 7 images). The two values have the same general trend: defects with larger surface height disturbances typically produce greater phase changes in the aerial image. Yet in many cases, we observe a significant phase difference that can be as large as 0.349 rad (20.0°). Part of the difference that we observed might be due the uncertainty in the AFM measurement, which is difficult to estimate from the data we have available.

As an example let's consider one of the pit defects that we inspected with an AFM depth of 5.85 nm. For this defect we observed the highest phase difference between the AFM prediction and the reconstruction, $\Delta p = 0.349$ rad. If we assume a Gaussian model for this defect, we can define peak phase in the aerial image as S($NA, p_0, FWHM$) where p_0 is the peak phase of the defect obtained from Eq. 9. The AFM height error Δh that could account for the observed phase difference is given by:

$$\Delta h = \frac{\lambda \cdot \Delta p}{4\pi} \left(\frac{\partial S}{\partial p_0} \right)^{-1} . \tag{10}$$

The approximate value of the partial derivative of S for the defect in question can be evaluated from fig. 2 as the slope of the 0.25 NA curve measured at $p_0 = 5.486$ rad and is equal to 0.55. The equivalent AFM height error is then $\Delta h = 0.68$ nm. Part of the phase difference that we observe can be accounted for as the error that we make assuming that the phase of the defect is given only by the local surface height change measured with the AFM.

4. CONCLUSION

The improved multi-image phase reconstruction algorithm that we have developed shows superior noise and solution stability performance relative to the two-image method that we described previously. The two-image method may contain a high correlation between the longitudinal step size and the spatial frequency resolution; this behavior could be considerably different in the improved approach, and deserves further study.

The multi-image method combines a greater amount of image data and searches for a self-consistent solution from a through-focus image series. Our analysis shows a significant reduction in the expected average RMS phase error with respect to the two-image algorithm. In the specific case shown in Fig. 5, for an image with a photon density of 100 photons/pixel, we observe an order of magnitude improvement switching two images to seven. Simulations with coherent illumination showed that there is an advantage to using a larger number of images in the reconstruction; however, this result may have limitations in the case of partially coherent illumination. The effect of partial coherence in the phase reconstruction is currently under investigation.

Applying the multi-image phase reconstruction method to EUV phase-defect images revealed another interesting result. The aerial-image phase estimated from the AFM defect-height profiles does not necessarily match the phase calculated from the multi-image reconstruction algorithm. Beyond having the same general trend, most of the defects show a significant difference between the two calculations. Part of this difference might be due to the uncertainty on the AFM data. On the other hand it is well known that the field reflected by the mask depends on the whole multilayer structure. A buried defect with an imperceptible top surface height profile can induce a significant phase change; and a defect near the surface can cause a large bump with a small phase change.

Given the challenge of characterizing EUV defects for mask repair and defect mitigation, we believe that image-based phase reconstruction methods can deepening our understanding of mask defects and serve as feedback to improve overall mask quality. Such analysis can also be applied to refine phase-shifting mask manufacturing techniques that could be used in the future. A reliable measurement of the aerial image' complex amplitude, could also improve the state of the art defect correction techniques.[14]

ACKNOWLEDGMENTS

REFERENCES

[1] Mochi, I., Goldberg, K. A., La Fontaine, B. , Tchikoulaeva, A., Holfeld, C., "Actinic imaging of native and programmed defects on a full-field mask," Proc. SPIE, 7636, 76361A (2010).

[2] Mochi, I., Goldberg, K. A. and Huh, S., "Actinic imaging and evaluation of phase structures on extreme ultraviolet lithography masks," J. Vac. Sci. Technol. B 28, C6E11 (2010).

[3] Gerchberg, R. W. and Saxton, W. O., "A practical algorithm for the determination of the phase from image and diffraction plane pictures," Optik 35, 237 (1972).

[4] Von Bunau, R. M., Fukuda, H. and Terasawa, T., "Phase Retrieval from Defocused Images and Its Applications in Lithography," Jpn. J. Appl. Phys., Part 1 36, 7494 (1997).

[5] Goldberg, K. A., Naulleau, P. P., Barty, A., Rekawa, S. B., Kemp, C. D., Gunion, R. F., Salmassi, F., Gullikson, E. M., Anderson, E. H. and Han, H.-S., "Performance of actinic EUVL mask imaging using a zoneplate microscope," Proc. SPIE 6730, 67305E (2007).

[6] Goldberg, K. A., Naulleau, P., Mochi, I., Anderson, E. H., Rekawa, S. B., Kemp, C. D., R. F. Gunion, Han, H.-S. and Huh, S., "Actinic extreme ultraviolet mask inspection beyond 0.25 numerical aperture," J. Vac. Sci. & Technol. B 26 (6), 2220 (2008).

[7] Goldberg, K. A., Mochi, I. and Huh, S., "Collecting EUV mask images through focus by wavelength tuning," Proc. SPIE 7271, 72713N (2009).

[8] Gullikson, E. M., Cerjan, C., Stearns, D. G., Mirkarimi, P. B. and Sweeney, D. W., "A practical approach for modelling EUVL mask defects," J. Vac. Sci. Technol. B 20, 81 (2002).

[9] Ivanov, V., Sivokon, V., and Vorontsov, M., "Phase retrieval from a set of intensity measurements: theory and experiment," *J. Opt. Soc. Am. A ,* 9 (9), 1515 (1992).

[10] Geary, J. M., [Introduction to Lens Design: With Practical Zemax Examples], Willmann-Bell. (2002).

[11] Naulleau, P., Niakoula, D. and Zhang, G., "System-level line-edge roughness limits in extreme ultraviolet lithography, J. Vac. Sci. & Technol. B 26 (6), 1289–93 (2008).

[12] George, S. A., Naulleau, P. P., Salmassi, F, Mochi, I., Gullikson, E. M., Goldberg, K. A. and Anderson, E. H., "Extreme ultraviolet mask substrate surface roughness effects on lithographic patterning," Journal of Vacuum Science and Technology B 28 (6), (2010).

[13] Wintz, D. T., Goldberg, K. A., Mochi, I. and Huh, S., "Photon flux requirements for EUV-reticle imaging microscopy in the 22- and 16-nm nodes," Proc. SPIE 7636, 76362L-1-10 (2010).

[14] Clifford, C. H., Chan, T. T. and Neureuther, A. R., "Compensation methods for buried defects in extreme ultraviolet lithography masks," J. Vac. Sci. Technol. B 29, 011022 (2011).